

Demystifying Pseudo-LiDAR for Monocular 3D Object Detection

Andrea Simonelli¹, Samuel Rota Bulò², Lorenzo Porzi², Peter Kontschieder², Elisa Ricci¹

¹University of Trento, ¹Fondazione Bruno Kessler, ²Facebook

Abstract

Pseudo-LiDAR-based methods for monocular 3D object detection have generated large attention in the community due to performance gains showed on the KITTI3D benchmark dataset, in particular on the commonly reported validation split. This generated a distorted impression about the superiority of Pseudo-LiDAR approaches against methods working with RGB-images only. Our first contribution consists in rectifying this view by analysing and showing experimentally that the validation results published by Pseudo-LiDAR-based methods are substantially biased. The source of the bias resides in an overlap between the KITTI3D object detection validation set and the training/validation sets used to train depth predictors feeding Pseudo-LiDAR-based methods. Surprisingly, the bias remains also after geographically removing the overlap, revealing the presence of a more structured contamination. This leaves the test set as the only reliable mean of comparison, where published Pseudo-LiDAR-based methods do not excel. Our second contribution brings Pseudo-LiDAR-based methods back up in the ranking with the introduction of a 3D confidence prediction module. Thanks to the proposed architectural changes, our modified Pseudo-LiDAR-based methods exhibit extraordinary gains on the test scores (up to $\approx +8\%$ 3D AP).

1. Introduction

3D object detection provides information about pose, location and category of an object in 3D space, making it an enabling technology for applications like autonomous driving or augmented reality. To obtain accurate localisation performance, existing solutions rely on depth information inferred from stereo cameras or derived from Light Detection and Ranging (LiDAR) sensors. The downsides of both variants are an increase of costs, the necessity of involved recalibration routines and the inhibition of the product design form factors due to physical fabrication constraints.

To combat these issues, an emerging branch of 3D object

¹<https://kepler.gl/policy/>, <https://www.mapbox.com/about/maps/>, <http://www.openstreetmap.org/copyright>, <https://www.mapbox.com/map-feedback/>

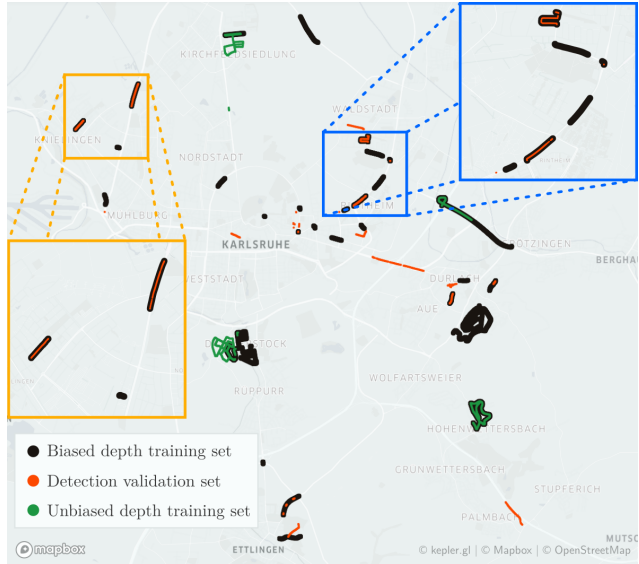


Figure 1: We analyze the cause of the performance bias of monocular Pseudo-LiDAR-based (PL) methods, which consists in a substantial drop between the results on the KITTI3D validation and test set. We show that this bias is due to the fact that the depth estimators on which PL methods heavily rely have been **trained** on a depth training set (black lines) which *includes* $\approx 30\%$ of the detection validation set data (red lines). We propose to solve this bias by creating an alternative *unbiased* depth training set (green lines) which eliminates the overlap as well as introduces a geographical distance w.r.t. detection validation data ¹.

detection methods is entirely based on monocular cameras [1, 10, 19, 20, 25, 27, 29]. Monocular cameras are a cheap alternative to the expensive LiDAR or stereo setups, but at the same time incur a substantially increased algorithmic complexity due to the absence of depth observations. Indeed, accurate estimation of an objects' distance to the camera is the most difficult task in monocular, image-based 3D object detection, rendering it an ill-posed problem. Despite the development of methods which focus on increasing the generalization with respect to distance [1, 27], monocular image-based methods still lag far behind their LiDAR or stereo-based counterparts.

A recent line of works [20, 31] leveraged CNNs for image-based depth predictions as depth substitute in monocular 3D object detection algorithms. Pseudo-LiDAR (PL) [29, 32] was promoted as a particularly effective depth representation, reporting impressive results on the challenging KITTI3D benchmark dataset. It essentially mimics a LiDAR signal for a RGB image by projecting each 2D pixel from its corresponding, estimated depth map into 3D space. With the resulting 3D point cloud, the 3D detection task is usually approached by applying *state-of-the-art* LiDAR-based (and thus 3D point-based) detection algorithms. PatchNet [18] has recently refuted 3D points as the source of PL’s effectiveness by providing an equivalently performing implementation based on stacking 3D world coordinates as 2D maps. While this eliminates the claims of PL being advantageous due to its 3D point-based representation, their ablations confirmed the importance of operating on transformed 2D image coordinates incorporating camera intrinsics (focal length and principal point).

In this paper we argue that PL-based approaches, and more in general approaches that take depth in input, have introduced a distorted perception in the research community about their performance in the monocular setting, against other state-of-the-art methods that use RGB-images only. The reason is twofold. First, all PL-based works reported scores only on the KITTI3D benchmark dataset.¹ Second, we discovered an issue in the evaluation pipeline adopted for this specific benchmark by *all* PL-based methods, which artificially leads to performance gains on the validation set as opposed to other, non-depth-based competitors. This bias can be essentially attributed to the way depth estimation algorithms have been trained before generating input to PL-based methods. Indeed, depth estimation algorithms were trained by including $\approx 30\%$ of the *validation* set data used for 3D object detection, resulting in significantly skewed validation performance scores, and diverting researcher’s attention from methods falling behind because of this bias. This particular, biased depth estimation model was subsequently used for all follow-up PL-based publications.

First contribution. Despite the existence of the bias has been mentioned, en passant, in the original PL paper [29], the community has not given yet the deserved attention to this issue. A first contribution of this paper is an in-depth investigation of the source of the bias by performing targeted experiments. We confirm that the bias exists in a significant extent. In an attempt to eliminate the source of the bias, we have created new training/validation splits for the upstream monocular depth estimation task by keeping sufficient geographic margin to the 3D object detection training and validation splits (see Fig. 1). To our great surprise, we found that this is not enough to get rid of the intrinsic

¹Some even solely provided results on the *validation* set, without reporting performance on the official KITTI3D test set [28, 29].

bias that affects PL-based methods on the validation set of the KITTI3D benchmark, revealing the presence of a more structured type of contamination. We also show that the test set is likely not affected by the same bias, thus preserving its value for the sake of fair comparisons.

Second contribution. The outcome of the comparison of PL-based methods against direct RGB-based methods in monocular 3D object detection on the KITTI3D benchmark is favouring more the latter ones, if we focus on test set results and if we factor in the amount of additional information and indirect model parameters that power PL-based methods. On the flip side, we found that published PL-based methods are potentially penalized by the lack of a proper 3D confidence score that is a fundamental component of many state-of-the-art RGB-only methods. As our second contribution, we endow PL-based methods with a mechanism for predicting a 3D confidence score, which gives remarkable boosts for both, the (biased) validation scores and the test scores of PL-based methods, surpassing the performance of previous state-of-the-art methods.

2. Related Works

Current approaches for monocular 3D object detection can be roughly divided in two categories: RGB-only methods, which directly address the ill-posed problem of the object’s distance estimation, and Pseudo-LiDAR (PL) methods, which leverage from automatically estimated depth maps or point clouds to recover the distance information.

Monocular RGB-only 3D detectors. Earlier approaches for monocular RGB-only 3D detection such as SSD-6D [11] and Deep3DBox [21] build on top of state of the art deep architectures for 2D detection, and exploit information from projective geometry to estimate the 3D pose and position of the objects in the scene. Mono3D [2] develops from the idea of generating 3D proposals and scoring them according to several cues, such as semantic segmentation features, object contour, and location priors. OFT-Net [24] operates by considering an orthographic feature transform to map a 2D feature map to bird-eye view. MonoGRNet [23] simultaneously estimates 2D bounding boxes, instance depth, 3D location of objects and local corners. GS3D [14] exploits an off-the-shelf 2D object detector and efficiently computes a coarse cuboid for each predicted 2D box, which is then refined to estimate the 3D bounding box. MonoPSR [12] jointly leverages 3D proposals and scale and shape estimation to accurately predict 3D bounding boxes from 2D ones. Recently, few works have proposed single-stage deep architectures [1, 27]. M3D-RPN [1] generates 2D and 3D object proposals simultaneously and exploits a post-processing optimisation and a depth-aware network to improve localization accuracy. MoVi-3D [27] is a lightweight architecture which exploits automati-

cally generated virtual views where the object appearance is normalized with respect to distance to facilitate the detection task. Other works such as MonoDIS [25] propose to improve both training convergence and detection accuracy of 3D detection networks by considering loss disentanglement. Using a similar idea, Liu *et al.* [17] propose SMOKE, a deep architectures which predicts 3D bounding boxes by relying on key-point estimation as an intermediate task.

Pseudo-LiDAR based 3D detectors. A second category of works exploit external data and network models to generate depth maps from the RGB input as an intermediate step for 3D detection. For instance, ROI-10D [20] introduces a loss to minimize the misalignment of 3D bounding boxes and exploits depth maps inferred with SuperDepth [22]. A disparity prediction module is considered in [31] and integrated into a network composed of two parts: one that generates 2D region proposals, and another that predicts of 3D object location, size and orientation. Pseudo-Lidar [29] introduces the simple idea of interpreting depth maps as 3D point clouds, which are then fed to state-of-the-art LiDAR-based 3D object detectors. Pseudo-Lidar++ [32] improves the accuracy in the localisation of faraway objects by adapting a stereo network architecture and deriving a loss function for direct depth estimation. AM3D [19] proposes to integrate complementary RGB features into the PL pipeline and introduces a specific module to map the 2D image data to the 3D point cloud. PatchNet [18] analyses the effect of depth data representation on performances and improves over previous PL models by integrating the 3D coordinates as additional channels of input data.

3. Preliminaries

We start with reviewing the monocular 3D object detection task and introducing the KITTI dataset [9] – the most influential benchmark to assess the performance of 3D detection methods. Our ablation study on KITTI details performance of state-of-the-art 3D object detection methods, and is highlighting the crucial role of depth estimation.

3.1. Monocular 3D Object Detection

The monocular 3D object detection task consists in detecting and localizing all the visible objects of interest (*e.g.* cars) by means of 3D bounding boxes given a single RGB image as input. Localization must be done in 3D space, properly estimating the 3D coordinates (in meters) of the center of the object $O_i = (X_i, Y_i, Z_i)$, where X_i, Y_i are related to the horizontal and vertical translations, respectively, and Z_i is the distance of the object’s center from the camera. The localization also includes the estimation of the object’s metric shape $S_i = (H_i, W_i, L_i)$ representing the object’s height, width and length, as well as the object’s rotation R_i w.r.t. the camera reference system. The detection requires

also to estimate a confidence value C_i which generally reflects the quality and determines how confident the detector is about the particular 3D detection. In this monocular setting, it is common to assume to have a calibrated camera and to know the corresponding intrinsic camera parameters.

3.2. The KITTI Dataset

The KITTI Dataset comprises a broad collection of data from street-level sequences, captured with a multi-sensor setup in the city of Karlsruhe (Germany) in 2011. The remarkable diversity of the sensors enabled many benchmarks, including *3D object detection* and *depth estimation*, which are most relevant for this work.

KITTI 3D object detection benchmark (KITTI3D). To our knowledge, all 3D object detection methods, and in particular monocular image-based ones, adopted KITTI3D as their predominant, and usually exclusive, testing field. The KITTI3D benchmark is composed of an official *training* and *testing* split, comprising 7481 and 7518 images, respectively. Following Chen *et al.* [3], it is common to split the training set into *unofficial* training and validation splits, with 3712 and 3769 images, respectively. KITTI provides 2D and 3D bounding box annotations for *Cars*, *Pedestrians* and *Cyclists*, and each box is assigned to one of the *difficulty* levels *Easy*, *Moderate* or *Hard*, depending on the object’s 2D height (\approx object’s distance), degree of occlusion, and truncation. Category *Car* comprises $\approx 83\%$ of the annotations, and is present in $\approx 94\%$ of the training images, while only $\approx 25\%$ and $\approx 13\%$ include a *Pedestrian* or *Cyclist* annotation, respectively. For this reason, many works exclusively evaluate on the *Car* class. KITTI3D adopts two main evaluation metrics, *i.e.*, *3D Average Precision (3D AP)* and *Bird’s Eye View Average Precision (BEV AP)*. As reported in [26], $AP|_{40}$ is the only legitimate 3D detection AP score, deprecating the previously used $AP|_{11}$ score.

Depth prediction benchmark. The KITTI depth prediction benchmark offers *official* training and testing splits, but it is common to split [7] the training data into *unofficial* training and validation sets of 23488 and 697 images, respectively. Depth prediction methods are inferring pixel-specific distance estimates w.r.t. the camera and are evaluated with several metrics like *Absolute Relative Error (AbsRel)*, *Squared Relative Error (SqRel)*, etc.

3.3. The Crucial Role of Depth

We proceed with an *oracle* analysis demonstrating that depth is what matters most in monocular 3D object detection. Following the definitions in Sec. 3.1, we used KITTI3D predictions of state-of-the-art monocular 3D object detection methods [1, 18, 25, 29] and compared their 3D object detection performances by *substituting* sub-task predictions (*e.g.* *depth*) with their corresponding ground-truth values. *E.g.*, we matched the predictions of each

Method	Oracle sub-task	3D AP ↑			BEV AP ↑		
		Easy	Mod.	Hard	Easy	Mod.	Hard
M3D-RPN [1]	—	12.78	10.36	8.07	18.69	14.57	11.09
	\hat{R}	14.71	11.78	9.26	20.54	16.37	13.32
	$H\hat{W}L$	13.47	10.52	8.26	19.84	14.97	12.05
	$\hat{X}\hat{Y}$	22.63	17.47	13.48	27.61	20.80	16.35
MonoDIS [26]	\hat{Z}	34.53	28.35	22.51	46.72	38.98	32.01
	—	16.71	12.32	10.58	24.56	18.48	16.23
	\hat{R}	17.27	12.76	11.45	24.60	18.83	16.50
	$H\hat{W}L$	16.75	12.56	11.29	24.87	18.91	16.51
Wang <i>et al.</i> [29]	$\hat{X}\hat{Y}$	29.59	22.17	19.31	36.74	26.23	22.97
	\hat{Z}	45.99	38.02	33.48	64.58	54.26	48.42
	—	23.71	12.40	10.61	31.32	18.44	15.30
	$\hat{H}\hat{W}L$	24.04	13.39	11.13	32.52	19.74	16.66
PatchNet [18]	$\hat{X}\hat{Y}$	25.73	14.50	11.64	33.66	20.36	17.02
	\hat{Z}	53.71	35.15	29.38	67.07	50.27	43.34
	—	31.15	16.23	13.49	40.81	23.42	19.70
	\hat{R}	31.60	17.43	14.58	41.19	24.78	20.25
PatchNet [18]	$H\hat{W}L$	34.19	19.01	15.58	43.41	25.39	20.67
	$\hat{X}\hat{Y}$	44.23	25.62	21.76	50.06	30.00	24.93
	\hat{Z}	59.81	41.93	35.94	71.29	55.68	48.71

Table 1: Oracle analyses. We computed the 3D object detection results of state-of-the-art methods by substituting selected predicted components (*Oracle*) with their corresponding ground-truth value (*e.g.* \hat{Z}). All the methods show the same pattern, highlighting that the distance estimation component (Z) is by-far the most crucial. Results have been computed on the widely adopted KITTI3D [9] validation split defined in [3] for the class *Car* with the official $AP|_{R_{40}}$ metric.

method and 3D bounding box B with the best-matching ground-truth bounding box \hat{B} . Then, we substitute a component of the predicted 3D bounding box (*e.g.* Z) with its corresponding ground truth (\hat{Z}), and report the resulting oracle scores in Tab. 1. The table shows that certain sub-tasks like *rotation* (R) and *shape* (W, H, L) prediction, despite the substitution with ground-truth values, do not significantly improve performance. In contrast, substituting the predicted *depth* estimation (Z) with ground truth improves substantially, meaning that *depth* is by-far the most crucial component for 3D object detection. Note that in our tables we use the \uparrow or \downarrow symbols to mark metrics where larger or smaller values are better, respectively.

4. The Bias in Pseudo-LiDAR Experiments

With depth identified as most critical component in monocular 3D detection works, it becomes obvious that PL-based methods are particularly sensitive to inputs from depth estimators trained in a biased way.

4.1. The Source of the Bias

To our knowledge, all PL-based methods published so far were exclusively evaluated on the KITTI3D [9] dataset which, as described in Sec. 3.2, shares data among several

benchmarks like 3D object detection and depth prediction. With the advent of PL, it is however paramount to identify potential sources of cross-pollination in task-specific dataset splits. Our investigations showed that previous, PL-based works [29, 32, 18] were built on top of DORN [8], *i.e.* a state-of-the-art depth estimator, that in turn however included a majority of images from the detection *validation* set during its training. Specifically, we found **1226/3769 (32.5%)** images to be shared between the widely adopted Eigen *et al.* training split [7] for depth estimation and the commonly used Chen *et al.* [3] validation split for 3D object detection. When adding also the images belonging to the same capturing sequence, the numbers slightly increase to 1258/3769 (33.4%). We illustrate the full extent of the contamination in Fig. 1, plotting GPS positions and hence the overlap of the different splits (Eigen *et al.* depth training split in black; Chen *et al.* validation split for 3D object detection in red). Obviously, this overlap in the datasets will lead to biased results in downstream, PL-based methods, greatly simplifying the task of depth estimation for the 3D object detector. Even though the original PL paper [29] already mentioned this issue, all subsequent works have continued to compare their PL-based results in the same manner, thus severely distorting the view on other works from the (monocular) 3D object detection domain.

In Tab. 3, we show the effect of the contamination on the validation and test scores for the original PL method from Wang *et al.* [29] and the more recent PatchNet [18]. The rows corresponding to *Eigen train* are based on biased depth in input, which was generated by a BTS [13] depth estimator trained on the Eigen *et al.* split. The huge performance drops (up to 17.6 AP) between obtained validation and test scores strongly underline the relevance of the bias issue discussed here.

4.2. Can the Bias be Removed?

As explained in the previous section, it is beyond doubt that a contamination exists between the depth training and detection validation sets used by PL-based methods. However, to further support the hypothesis that this contamination causes a bias in the KITTI3D validation scores, we take one step further: we create an *unbiased* depth training split.

Unbiased depth training split. The main objective we pursue with our unbiased depth training split is to avoid including any image which is also contained in the detection validation set. Additionally, to avoid indirect contamination due to spatial correlations, we also enforce significant spatial separation between the two. We exploit the GPS information included in the available KITTI Benchmark data, and define two separation criteria. We withhold all images i) captured closer than 50m from any training or validation detection image, and ii) belonging to any of the detection sequences. Due to the very limited amount of

Training set	Validation Set	Biased	$d_1 \uparrow$	$d_2 \uparrow$	$d_3 \uparrow$	$AbsRel \downarrow$	$SqRel \downarrow$	$RMSE \downarrow$	$SILog \downarrow$
Eigen train.	Eigen valid.	No	0.908	0.967	0.983	0.084	0.557	4.003	16.577
Eigen train.	Detec. train.	Yes	0.926	0.971	0.985	0.067	0.504	3.806	15.250
Eigen train.	Detec. valid.	Yes	0.920	0.967	0.982	0.072	0.495	3.838	16.063
Unbiased train.	Unbiased valid.	No	0.904	0.975	0.991	0.093	0.494	3.627	14.019
Unbiased train.	Detec. train.	No	0.858	0.962	0.987	0.111	0.715	4.830	15.960
Unbiased train.	Detec. valid.	No	0.872	0.964	0.988	0.105	0.629	4.429	15.872

Table 2: *Biased vs. Unbiased* Depth estimation results with BTS on KITTI, computed w.r.t. ground-truth depth obtained from LiDAR scans.

3D Object Detector	Depth Estimator	Depth Training Set	Biased Depth	<i>Validation set</i> 3D AP \uparrow			<i>Test set</i> 3D AP \uparrow		
				Easy	Mod.	Hard	Easy	Mod.	Hard
Wang <i>et al.</i>	BTS	Eigen train. Unbiased train.	Yes	24.47	13.40	10.92	9.87	6.40	5.46
	BTS		No	17.20	9.35	7.57	10.76	6.86	5.93
PatchNet	BTS	Eigen train. Unbiased train.	Yes	31.60	18.22	15.10	14.00	8.70	7.39
	BTS		No	20.79	10.55	8.90	10.88	7.42	6.51

Table 3: *Biased vs. Unbiased* Pseudo-LiDAR results on KITTI3D validation and official benchmark, class *Car*, official $AP|_{R_{40}}$ metric.

available data, we apply both (i) and (ii) to the selection of the depth training set, and only (ii) to the selection of the validation set. From a total available amount of 47962 images, the aforementioned filtering process yields 13887 images for the training set and 5058 images for the validation set. To avoid redundancy in the validation set we further sub-sample it to a total of 1000 images. Our new data split is visualised in Fig. 1 (green markers) and shows that overlaps between depth training (Eigen *et al.* [7], black markers) and object detection validation (red markers) splits are eliminated, and additionally a safety margin is implemented.

Validating the unbiased split. To verify whether our novel split is truly unbiased, we use it to train a depth estimation model. Due to the fact that no open-source code is publicly available for DORN [8], *i.e.* the model commonly used by PL-based methods, we instead adopt the recently published state-of-the-art depth estimator BTS [13].² Then, we use this model to generate PL inputs to train monocular 3D detectors. In particular, we focus on two state-of-the-art PL methods, namely the one in Wang *et al.* [29]³ and the recent PatchNet [18]⁴, both providing open source code (re-implementation and official code, respectively). The results of this analysis, shown in Tab. 2 and Tab. 3, highlight the clear presence of bias in both depth estimation and 3D detection results. In particular, the depth metrics of the models trained on the Eigen *et al.* split (Eigen train.) exhibit significantly better performance on images from the detection validation set (Detec. valid.) compared to the ones trained with the unbiased depth split (Unbiased train.). At the same

time, each trained model performs well on its own validation set, thus revealing the presence of a bias. Similarly, in the 3D detection setting, PL-based methods trained with biased input depth reach significantly higher validation scores on all difficulty levels, while performing in proportion significantly worse on the test set. The huge gap that emerges between test and validations scores (up to 17.6 AP) is a clear evidence of the validation bias. On the other hand, the same models trained with unbiased depth in input exhibit a significant drop in the validation scores that is not reflected in the same proportion in the test set. This indicates that our initial hypothesis, about the bias being related to the overlap between the depth training set and the detection validation set was indeed correct and we managed to reduce the gap between validation and test with our unbiased version of the depth training split. It is worth mentioning that the drop in performance on the test set compared to the Eigen *et al.* split is probably attributed to the smaller set used to train the depth estimator.

Removing the bias. If we move back to the question that opened the section, whether it is possible to remove the bias that affects the PL-based methods on KITTI3D, unfortunately, we are still not entitled to give a positive answer. To our great surprise, despite the lack of geographical intersection between the depth and detection splits, the gap between validation and test results is still substantially higher (up to 10 AP) compared to the gap that methods using RGB-only inputs typically incur (\approx 3-5 AP). This is a clear indication that some more structured form of bias still exists that goes beyond the simple geographical reasoning we made to construct our unbiased split. On the other hand, the fact that published PL-based methods, or more in general methods

²[13]: <https://github.com/cogaplex-bts/bts>

³[29]: https://github.com/mileyan/pseudo_lidar

⁴[18]: <https://github.com/xinzhuma/patchnet>

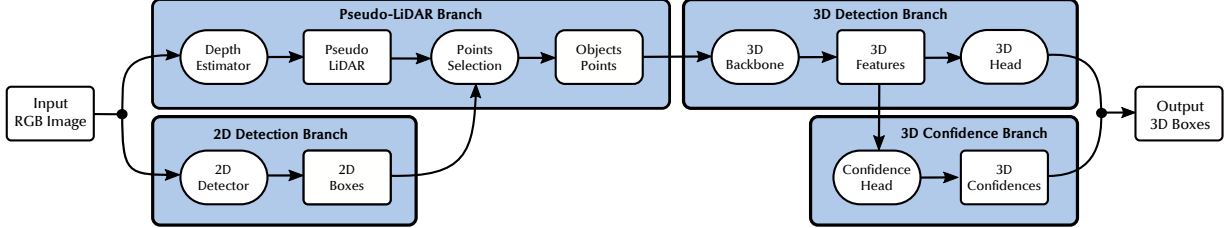


Figure 2: Architecture of a Pseudo-LiDAR-based method integrating the proposed 3D confidence component.

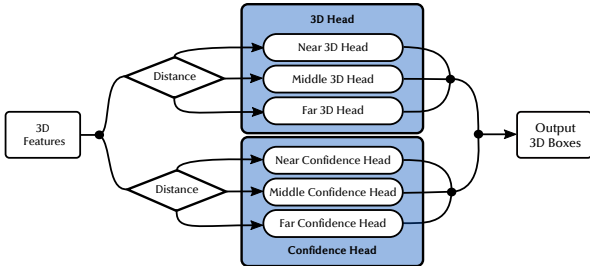


Figure 3: Example of final part of the architecture, where we added our proposed *Confidence Head* to the PatchNet [18] architecture.

that take depth in input, are not able to surpass the state-of-the-art RGB-based methods (see Tab. 6 first block) is an indication that the test set itself does not suffer from the same type of bias, thus preserving its validity for the sake of fair comparisons.

Despite lacking a complete explanation of the source of the bias affecting PL-based methods on KITTI3D, we believe our analysis could be a first step towards unbiasing PL-based methods and encourage the community to take the issue into account for future works. Indeed, any work exploiting depth information in input will be exposed to biases that this external source of data might introduce and care should be taken to avoid reporting comparative results if the bias is present.

5. 3D Confidence for PL-based Methods

The 3D object detection task, as described in Sec. 3.1, requires to associate each object with a 3D bounding box and a corresponding *confidence* value. This confidence should generally reflect the quality of the 3D bounding box and can be thought as a measure of how much the particular estimate is reliable. In datasets such as KITTI3D, this confidence takes an active role in the computation of the metrics (*e.g.* Average Precision). In light of this fact we observed that existing Pseudo-LiDAR methods *e.g.* [29, 18] do not perform the 3D confidence estimation *in any way* and rely on the class probability coming along with the 2D detections. By doing so, the confidence adopted by current PL-based

methods is actually agnostic to the quality of the 3D predictions and therefore not effective for the role it should take. On top of this, as shown in Fig. 5, we observed that 2D detectors are often too confident and therefore the need for a 3D confidence seems essential. For this reason, we propose to endow PL-based methods with the ability of estimating the 3D confidence of their predictions.

5.1. Confidence Estimation

In order to describe how the confidence is estimated we will now overview the general architecture used by PL-based methods *e.g.* [29, 18], subsequently detailing our changes. The architecture that is commonly adopted by state-of-the-art PL-based methods is depicted in Fig. 2 (excluding the 3D confidence branch, *i.e.* our contribution). This architecture can be divided into three main branches namely *2D Detection*, *Pseudo-LiDAR* and *3D Detection* which we will now describe in more detail.

2D detection component. Given an RGB image as input, a 2D detection method estimates the presence as well as position of objects of interest by means of 2D bounding boxes. It is very common to treat this part of the architecture as an independently trained block, leveraging the results of a state-of-the-art 2D detector *as-is*. Further details can be found in Wang *et al.* [29] or PatchNet [18].

Pseudo-LiDAR (PL) component. In this part of the architecture a depth estimation network (*e.g.* [8, 13]) assigns each pixel a depth estimate. Similarly to the 2D component, this one is independently trained and leverages a state-of-the-art depth estimator *as-is*. Given the estimated depth, each pixel is then projected in 3D to form the PL point cloud. The PL pointcloud is then processed by a *Points Selection* operation which initially selects the points inside each 2D bounding box and subsequently performs an additional filtering with the objective of discarding points that potentially do not belong to the object of interest (*e.g.* occlusions, road).

3D detection component. This block is responsible for the estimation of the output 3D bounding boxes, taking as input the selected PL points to perform a point-based 3D detection by means of an initial *3D Backbone* followed by a *3D*

Head. While our proposed method is not tied to a specific architecture, we focused on the model in Wang et al. [29] and PatchNet [18]. In [29] the *3D Backbone* consists of a series of fully-connected layers plus an additional one which implements the *3D Head*. In [18], the first set of fully-connected layers is replaced by a relatively shallow Convolutional Neural Network while the *3D Head* is composed of three different sets of fully-connected layers operating in different distance ranges, namely *Near* ($<30m$), *Middle* ($30\text{-}50m$) and *Far* ($>50m$). A detail of our PatchNet-based *3D Head*, excluding the *Confidence Head*, is shown in Fig. 3.

The next component is part of our contribution and endows the PL-based methods under consideration with the ability to predict a self-supervised 3D confidence.

Confidence head. The estimation of the 3D confidence, in order to be reliable and accurate, has to heavily rely on 3D-related features. For this reason we introduce an additional branch in the architecture, namely the *3D Confidence Branch*, which, as shown in Fig. 2, takes as input the set of *3D Features* computed by the *3D Backbone* and outputs the 3D confidence. The *3D Confidence Head* takes the same shape as the existing *3D Head* which, as explained in the previous section, is implemented with one set of fully-connected layers for Wang et al. [29] and three distance-specific fully-connected modules for PatchNet [18]. Differently from the *3D Head*, the proposed *3D Confidence Head* estimates a single value C_i , i.e. the confidence, for each object. The general architecture of our PatchNet-based *3D Head* and *3D Confidence Head* is shown in Fig. 3. Note that the proposed *Confidence Branch* requires minimal modifications to the original architecture, adds negligible computational complexity and inference time and is compatible with most Pseudo-LiDAR approaches.

Learning the 3D confidence. The 3D confidence should reflect the quality of the 3D detection. This has been taken into account in the design of the confidence head, as described above, and it is also enforced in the way the confidence is learned, as we describe below. Inspired by [25], we consider the 3D confidence score regression as a classification task with a binary cross-entropy loss, where the target probabilities are directly derived from the 3D bounding box losses via negative exponentiation. Given a 3D bounding box prediction B_i and the corresponding ground-truth \hat{B}_i , the loss for the 3D confidence prediction C_i^{3D} is given by

$$L_{\text{conf}}(C_i^{3D}|B_i, \hat{B}_i) = -T_i \log C_i^{3D} - (1 - T_i) \log(1 - C_i^{3D}),$$

where $T_i = e^{-\ell(B_i, \hat{B}_i)}$ is the target confidence and $\ell(B_i, \hat{B}_i)$ is the loss incurred by the bounding box prediction. By doing so, the confidence score is directly linked to the 3D detection loss, which is already a direct measure of the quality of the regressed 3D bounding boxes. Finally,

Method	Depth Estimator	3D AP		
		Easy	Mod.	Hard
Wang et al. + 3D Confidence	BTS Eigen	24.47	13.40	10.92
	BTS Eigen	32.44	20.84	17.26
PatchNet + 3D Confidence	BTS Eigen	31.60	18.22	15.10
	BTS Eigen	38.30	24.11	19.23

Table 4: Validation set $AP|_{R_{40}}$ ablation results on KITTI3D.

since the 2D confidence is already available and could be useful to filter our *e.g.* false-positives, our final confidence for an object O_i will be $C_i^{\text{out}} = C_i^{\text{2D}} \cdot C_i^{\text{3D}}$.

6. Experiments

Following the experimental protocol of the PL-based works (*e.g.* [29, 18]), we evaluate our method on the KITTI3D [9] benchmark focusing on the class *Car*. A description of the benchmark is given in Sec. 3.2. All the results presented and reported in this work have been computed with the official $AP|_{R_{40}}$ metric, which from October 2019 has been completely substituting the deprecated $AP|_{R_{11}}$ metric. The official $AP|_{R_{40}}$ solved a flaw in the previous metric that was biasing scores. Please refer to [25] for further details. Finally, in all our experiments we rely on the same 2D detections used by PatchNet [18].

Discussion of results. In Tab. 4 we investigate the influence of our proposed *3D Confidence* on the Pseudo-LiDAR methods of Wang et al. [29] and PatchNet [18]. In order to do so, we compute the 3D object detection metrics on the validation set of KITTI3D with the baseline methods as well as with the addition of the *3D Confidence Head* (+ 3D Confidence). As show in the table, we observe a major improvement on the 3D AP. This validates our hypothesis about the importance of having a 3D confidence prediction component in PL-based methods. In Tab. 6, we compare our results against the state of the art on the KITTI3D test set.⁵ Our variant of PatchNet surpasses the previous best by a large margin, establishing a new state-of-the-art. At the same time our variant of Wang et al. achieves the second best result on the Easy metric.

Implementation details. In this section we provide details about the implementation and information about the hyperparameters. Since our method is subdivided into multiple branches, we provide details of each one namely *2D Detection*, *Pseudo-LiDAR* and *3D Detection*.

In all our experiments, we trained our models on a single NVIDIA GTX 1080 Ti with 11GB of memory. We followed the schedules and hyperparameters choices of PatchNet [18]

⁵http://www.cvlibs.net/datasets/kitti/eval_object.php?obj_benchmark=3d



Figure 4: Qualitative results of our method with confidence scores of each detection. Top: We report the 2D confidence score that PL-based methods typically use. Bottom: We report the learned 3D confidence predicted by our method.

Method	Depth estimator	3D AP		
		Easy	Mod.	Hard
Wang et al. + 3D Confidence	BTS Eigen	14.17	8.47	7.29
	BTS Eigen	18.56	10.99	9.31
PatchNet + 3D Confidence	BTS Eigen	15.70	10.15	8.79
	BTS Eigen	23.66	13.25	11.23

Table 5: Test set $AP|_{R_{40}}$ ablation results on KITTI3D.

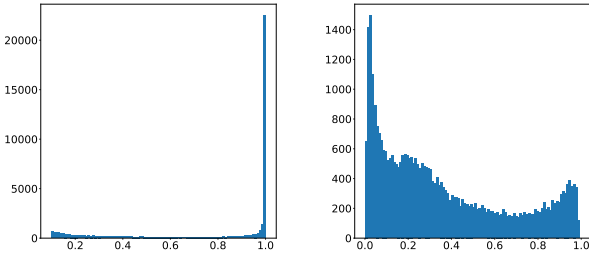


Figure 5: Histogram of our KITTI3D test set 2d confidences (left) and proposed 3D confidences (right).

or Wang et al. [29], with the only addition of the 3D Confidence loss which is given a weight of 1.0.

2D Detection. We do not train a 2D detector but instead rely on pre-computed 2D detections. In our experiments we used, for both validation and test set, the 2D detections used in PatchNet [18].

Pseudo-LiDAR. We took the open-source code of BTS [13] and selected the DenseNet161-based estimator. For our results on the Eigen et al. we used the model trained

Method	Input	3D AP		
		Easy	Mod.	Hard
OFTNet [24]	RGB	1.61	1.32	1.00
FQNet [16]	RGB	2.77	1.51	1.01
ROI-10D [20]	RGB	4.32	2.02	1.46
GS3D [14]	RGB	4.47	2.90	2.47
MonoGRNet [23]	RGB	9.61	5.74	4.25
MonoPSR [12]	RGB	10.76	7.25	5.85
Mono3D-PL [30]	Depth	10.76	7.50	6.10
SS3D [10]	RGB	10.78	7.68	6.51
MonoDIS [25]	RGB	10.37	7.94	6.40
M3D-RPN [1]	RGB	14.76	9.71	7.42
SMOKE [17]	RGB	14.03	9.76	7.84
MonoPair [4]	RGB	13.04	9.99	8.65
RTDM3D [15]	RGB	14.41	10.34	8.77
AM3D [19]	RGB+Depth	16.50	10.74	9.52
MoVi-3D [27]	RGB	15.19	10.90	9.26
PatchNet [18]	Depth	15.68	11.12	10.17
D4LCN [6]	RGB+Depth	16.65	11.72	9.51
MonoDIS [26]	RGB	16.50	<u>12.20</u>	<u>10.30</u>
Our Wang et al.	Depth	<u>18.56</u>	10.99	9.31
Our PatchNet	Depth	23.66	13.25	11.23

Table 6: Test set SOTA $AP|_{R_{40}}$ official results on KITTI3D. Methods ranked following KITTI3D Benchmark (*Moderate* 3D AP). Best scores in bold, runner-ups underlined.

by the authors. For the trainings on our novel *Unbiased* splits, we used the ImageNet [5] pre-trained model and followed the official schedule and hyperparameters with the exception of the reduction of the number of epochs from 50 to 24. This reduction is due to the fact that our novel training split ($\approx 13k$ images) is smaller than the Eigen et al. training split ($\approx 24k$ images).

3D Detection. The architecture of our proposed models,

i.e. the ones based on Wang et al. [29] and PatchNet [18], always follow the official one with the only exception of the introduction of our proposed *3D Confidence Head*. The implementation of this particular head closely follows the one of the respective 3D Head. In particular, for our implementation based on Wang et al [29] we introduced a series of three fully-connected layers with *512-D*, *512-D*, and *1-D* dimensions respectively. For the implementation of PatchNet [18] we introduced three distance-specific heads composed by a series of three fully-connected layers with *512-D*, *512-D*, and *1-D* dimensions respectively. We trained our model with the Adam optimizer with a learning rate of 0.001 and a batch size of 64 for 100 epochs, decreasing the learning rate by a factor of 0.1 at the 20th and 40th epoch.

7. Additional qualitative results

We provide additional qualitative results of our detections on KITTI3D.

We visualize results on the KITTI3D test set by superimposing our *PatchNet + 3D Confidence* 3d bounding box detections on the input RGB images, showing the corresponding confidence value of each detection. The images in Fig. 7,8 show that our proposed confidence reliably determines the overall quality of the predicted 3D bounding box. The confidence is in fact higher on nearer objects, *i.e.* where the estimation is more reliable, and seems to degrade with distance. We also included some failure cases in which our confidence is shown to be less reliable. In particular, we have identified some imprecise or empty detections that still have fairly high confidence.

We further provide a qualitative video⁶ by showing our predictions on complete *unbiased* sequences taken from the KITTI3D validation set. Unfortunately, it was not possible to provide videos on the KITTI3D test set sequences due to the unavailability of test set sequence information. In these videos we show our predictions in two different formats, as shown in Fig. 6. On the bottom part of the video we super-impose the bounding boxes with corresponding confidence score on each RGB image as done in the previous figures *e.g.* Fig. 7. In the top part of the video we visualize our detections on the rendered Pseudo-LiDAR pointcloud, where each point has been colored with its corresponding RGB value (if available), and consequently visualized our predicted 3d bounding-boxes in green. The predictions are computed for each frame in an independent manner, without exploiting temporal information in any way. The presence of black pixels (*e.g.* on top of objects) is due to the fact that we rendered the scene from a point-of-view which is different from the one of the KITTI3D RGB camera. This change of pose inevitably introduces these black pixels on regions

which were not visible from the RGB camera pose.

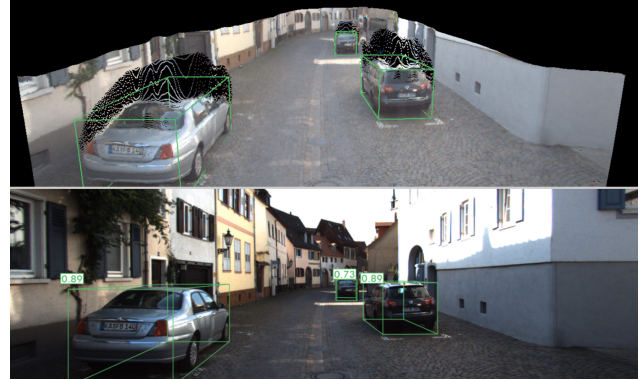


Figure 6: Example of single frame taken from our qualitative video on an unbiased KITTI3D validation sequence. Top: Visualization of our predictions on the colored Pseudo-LiDAR pointcloud. Bottom: Visualization of our predictions, with corresponding confidence score, on the input RGB image.

8. Conclusions

In this paper we have shown that all previously published Pseudo-LiDAR-based works suffer from a bias in the reported validation scores for the KITTI3D benchmark. The source of the issue is partially due to an overlap that exists between the training set used to train the upstream depth estimators, providing the depth in input to the PL-based methods, and the validation set used for 3D object detection. In an attempt to validate the hypothesis we constructed an unbiased training set for the depth estimators by ensuring geographical separation to the detection validation set. However we found that this is not sufficient to remove the bias in the validation set, which indicates the existence of a more structured nature of the issue. As a consequence, future works involving PL-based methods on KITTI3D should avoid comparative analysis against other methods using the validation set, but rather rely on the test set. In the second part of our work, we provided an architectural change to PL-based methods aimed at endowing them with the ability of predicting 3D confidences. We showed that with this simple change PL-based methods get remarkable improvements on the KITTI3D benchmark eventually establishing a new state of the art.

9. Acknowledgements

We thank Xinzhu Ma, Wanli Ouyang and Garrick Brazil for sharing their detections and for helpful discussions.

⁶<https://tinyurl.com/demystifyingpl>



Figure 7: Additional qualitative results of our 3d bounding box detections on the KITTI3D test set.



Figure 8: Additional qualitative results of our 3d bounding box detections on the KITTI3D test set.

References

- [1] Garrick Brazil and Xiaoming Liu. M3D-RPN: Monocular 3d region proposal network for object detection. In (*ICCV*), pages 9287–9296, 2019. [1](#), [2](#), [3](#), [4](#), [8](#)
- [2] Xiaozihi Chen, Kaustav Kundu, Ziyu Zhang, Huimin Ma, Sanja Fidler, and Raquel Urtasun. Monocular 3d object detection for autonomous driving. In (*CVPR*), 2016. [2](#)
- [3] Xiaozihi Chen, Kaustav Kundu, Yukun Zhu, Andrew G. Berneshawi, Huimin Ma, Sanja Fidler, and Raquel Urtasun. 3d object proposals for accurate object class detection. In *NIPS*, 2015. [3](#), [4](#)
- [4] Yongjian Chen, Lei Tai, Kai Sun, and Mingyang Li. Monopair: Monocular 3d object detection using pairwise spatial relationships. In *CVPR*, pages 12093–12102, 2020. [8](#)
- [5] J. Deng, W. Dong, R. Socher, L.-J. Li, K. Li, and L. Fei-Fei. ImageNet: A Large-Scale Hierarchical Image Database. In (*CVPR*), 2009. [8](#)
- [6] Mingyu Ding, Yuqi Huo, Hongwei Yi, Zhe Wang, Jianping Shi, Zhiwu Lu, and Ping Luo. Learning depth-guided convolutions for monocular 3d object detection. In *CVPR*, pages 11672–11681, 2020. [8](#)
- [7] David Eigen and Rob Fergus. Predicting depth, surface normals and semantic labels with a common multi-scale convolutional architecture. In (*ICCV*), pages 2650–2658, 2015. [3](#), [4](#), [5](#)
- [8] Huan Fu, Mingming Gong, Chaohui Wang, Kayhan Batmanghelich, and Dacheng Tao. Deep Ordinal Regression Network for Monocular Depth Estimation. In (*CVPR*), 2018. [4](#), [5](#), [6](#)
- [9] Andreas Geiger, Philip Lenz, and Raquel Urtasun. Are we ready for autonomous driving? The kitti vision benchmark suite. In *CVPR*, 2012. [3](#), [4](#), [7](#)
- [10] Eskil Jorgensen, Christopher Zach, and Fredrik Kahl. Monocular 3d object detection and box fitting trained end-to-end using intersection-over-union loss. In *CVPR*, 2019. [1](#), [8](#)
- [11] Wadim Kehl, Fabian Manhardt, Federico Tombari, Slobodan Ilic, and Nassir Navab. SSD-6D: Making rgb-based 3d detection and 6d pose estimation great again. In (*ICCV*), October 2017. [2](#)
- [12] Jason Ku, Alex D. Pon, and Steven L. Waslander. Monocular 3d object detection leveraging accurate proposals and shape reconstruction. In (*CVPR*), 2019. [2](#), [8](#)
- [13] Jin Han Lee, Myung-Kyu Han, Dong Wook Ko, and Il Hong Suh. From big to small: Multi-scale local planar guidance for monocular depth estimation. *arXiv:1907.10326*, 2019. [4](#), [5](#), [6](#), [8](#)
- [14] Buyu Li, Wanli Ouyang, Lu Sheng, Xingyu Zeng, and Xiaogang Wang. Gs3d: An efficient 3d object detection framework for autonomous driving. In (*CVPR*), 2019. [2](#), [8](#)
- [15] Peixuan Li, Huaici Zhao, Pengfei Liu, and Feidao Cao. Rtm3d: Real-time monocular 3d detection from object keypoints for autonomous driving. In *ECCV*, 2020. [8](#)
- [16] Lijie Liu, Jiwen Lu, Chunjing Xu, Qi Tian, and Jie Zhou. Deep fitting degree scoring network for monocular 3d object detection. *CoRR*, abs/1904.12681, 2019. [8](#)
- [17] Zechen Liu, Zizhang Wu, and Roland Tóth. SMOKE: Single-stage monocular 3d object detection via keypoint estimation. *CoRR*, abs/2002.10111, 2020. [3](#), [8](#)
- [18] Xinzhu Ma, Shinan Liu, Zhiyi Xia, Hongwen Zhang, Xingyu Zeng, and Wanli Ouyang. Rethinking pseudo-lidar representation. In (*ECCV*), 2020. [2](#), [3](#), [4](#), [5](#), [6](#), [7](#), [8](#), [9](#)
- [19] X. Ma, Z. Wang, H. Li, P. Zhang, W. Ouyang, and X. Fan. Accurate monocular object detection via color- embedded 3d reconstruction for autonomous driving. In *ICCV*, 2019. [1](#), [3](#), [8](#)
- [20] Fabian Manhardt, Wadim Kehl, and Adrien Gaidon. ROI-10D: Monocular lifting of 2d detection to 6d pose and metric shape. In (*CVPR*), 2019. [1](#), [2](#), [3](#), [8](#)
- [21] Arsalan Mousavian, Dragomir Anguelov, John Flynn, and Jana Kosecka. 3d bounding box estimation using deep learning and geometry. In (*CVPR*), July 2017. [2](#)
- [22] Sudeep Pillai, Rares Ambrus, and Adrien Gaidon. Superdepth: Self-supervised, super-resolved monocular depth estimation. In *Proc. IEEE Intern. Conf. on Robotics and Automation (ICRA)*, 2019. [3](#)
- [23] Zengyi Qin, Jinglu Wang, and Yan Lu. Monognnet: A geometric reasoning network for 3d object localization. In (*AAAI*), 2019. [2](#), [8](#)
- [24] Thomas Roddick, Alex Kendall, and Roberto Cipolla. Orthographic feature transform for monocular 3d object detection. *CoRR*, abs/1811.08188, 2018. [2](#), [8](#)
- [25] Andrea Simonelli, Samuel Rota Bulò, Lorenzo Porzi, Manuel López-Antequera, and Peter Koutschieder. Disentangling monocular 3d object detection. In (*ICCV*), pages 1991–1999, 2019. [1](#), [3](#), [7](#), [8](#)
- [26] Andrea Simonelli, Samuel Rota Bulò, Lorenzo Porzi, Manuel López-Antequera, and Peter Koutschieder. Disentangling monocular 3d object detection: From single to multi-class recognition. In *TPAMI*, 2020. [3](#), [4](#), [8](#)
- [27] Andrea Simonelli, Samuel Rota Bulò, Lorenzo Porzi, Elisa Ricci, and Peter Koutschieder. Towards generalization across depth for monocular 3D object detection. In *ECCV*, pages 9287–9296, 2020. [1](#), [2](#), [8](#)
- [28] Xinlong Wang, Wei Yin, Tao Kong, Yuning Jiang, Lei Li, and Chunhua Shen. Task-aware monocular depth estimation for 3d object detection. In (*AAAI*), 2020. [2](#)
- [29] Yan Wang, Wei-Lun Chao, Divyansh Garg, Bharath Hariharan, Mark Campbell, and Kilian Weinberger. Pseudo-lidar from visual depth estimation: Bridging the gap in 3d object detection for autonomous driving. In (*CVPR*), 2019. [1](#), [2](#), [3](#), [4](#), [5](#), [6](#), [7](#), [8](#), [9](#)
- [30] Xinshuo Weng and Kris Kitani. Monocular 3d object detection with pseudo-lidar point cloud. In (*ICCVW*), 2019. [8](#)
- [31] Bin Xu and Zhenzhong Chen. Multi-level fusion based 3d object detection from monocular images. In (*CVPR*), June 2018. [2](#), [3](#)
- [32] Yurong You, Yan Wang, Wei-Liu Chao, Divyansh Garg, Geoff Pleiss, Bharath Hariharan, Mark Campbell, and Kilian Q. Weinberger. Pseudo-lidar++: Accurate depth for 3d object detection in autonomous driving. *CoRR*, abs/1906.06310, 2019. [2](#), [3](#), [4](#)